Supporting Information for

Chemiresistive Sensing of Ambient CO_2 by an Autogenously Hydrated Cu_3(hexaiminobenzene)$_2$ Framework

*Ivo Stassen, Jin-Hu Dou, Christopher Hendon and Mircea Dincă**

Table of Contents

1. General Procedures and Experimental Details

1.1 Synthesis of 2D MOFs

All chemicals were utilized as obtained from commercial suppliers, or for the synthesized ligand precursors as obtained from the referenced procedure. Adapted version of the published procedures were used for preparation of Cu_3HIB_2,[1] Ni_3HIB_2,[1] Cu_3HITP_2,[2] Ni_3HITP_2,[3] and Cu_3HOTP_2.[4] The synthesis reactions starting from metal salts and the free ligands are described below. All prior steps, such as synthesis and purification of the ligands (HAB = hexa-aminobenzene; HATP = hexa-aminotriphenylene; HHTP = hexahydroxytriphenylene) were conducted in accordance with the reported procedures.

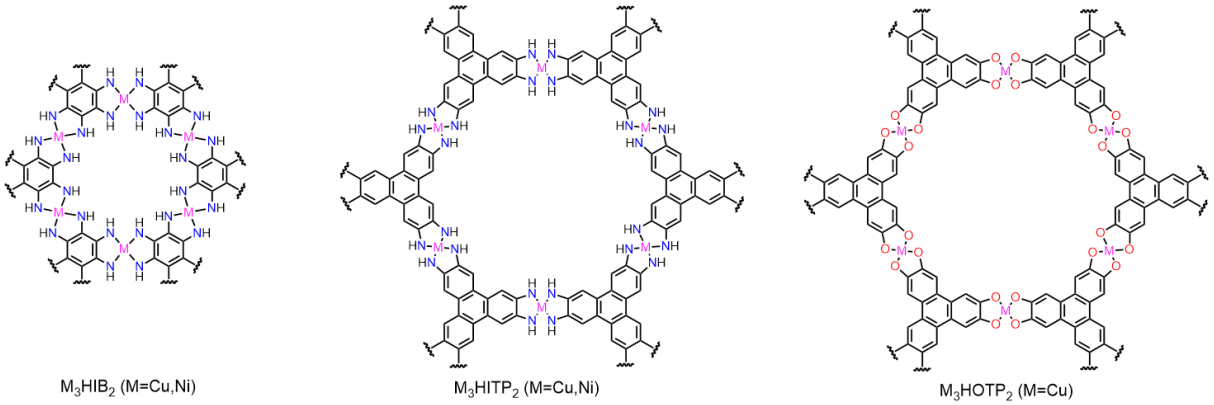

Cu_3HIB_2

A solution of 13.5 mg of $CuSO_4 \cdot 5H_2O$ (0.055 mmol) and 0.4 mL of 14M NH_4OH in 2 mL of degassed H_2O was added to a solution of 10 mg of HAB·3HCl (0.036 mmol) in 2 mL degassed H_2O in a 20 mL scintillation vial. The vial was loosely capped and kept at 65 °C in air for 2 hours without stirring. The product precipitated out as black solids. The mixture was centrifuged, decanted and washed with deionized 5 mL water for three times and then 5 mL methanol for another three times and then the solid product was kept in 3 mL methanol.

Ni_3HIB_2

A solution of 16.0 mg of $Ni(NO_3)_2 \cdot 6H_2O$ (0.055 mmol) and 0.4 mL of 14M NH_4OH in 2 mL of degassed H_2O was added to a solution of 10 mg of HAB·3HCl (0.036 mmol) in 2 mL degassed H_2O in a 20 mL scintillation vial. The vial was loosely capped and put under 65 °C for 2 hours without stirring. The product precipitated out as black solids. The mixture was centrifuged, decanted and washed with 5 mL deionized water for three times and then 5 mL methanol for another three times and then the solid product was kept in 3 mL methanol.

Cu_3HITP_2

A solution of 7.0 mg of CuSO4·5H2O (0.028 mmol) and 100 µl of 14M NH4OH in 2 mL of degassed H_2O was added to a solution of 10 mg of HATP·6HCl (0.019 mmol) in 2 mL degassed H_2O in a 20 mL scintillation vial. The vial was loosely capped and kept at 25 °C in air for 3 hours without stirring. The product precipitated out as black solids. The mixture was centrifuged, decanted and washed with 5 mL deionized water for three times and then 5 mL methanol for another three times and then the solid product was kept in 3 mL methanol.

Ni_3HITP_2
A solution of 16.5 mg (0.057 mmol) of $Ni(NO3)_2 \cdot 6H_2O$ and 0.4 mL of 14M NH_4OH in 2 mL of degassed H_2O was added to a solution of 10 mg (0.019 mmol) of HATP·6HCl in 2 mL of degassed H_2O in a 20 mL scintillation vial. The vial was loosely capped and put under 60 °C for 2 hours without stirring. The product precipitated out as black solids. The mixture was centrifuged, decanted and washed with 5 mL deionized water for three times and then 5 mL methanol for another three times and then the solid product was kept in 3 mL methanol.

Cu_3HOTP_2
A solution of 11.2 mg of $Cu(OAc)_2$ H_2O (0.056 mmol) in 1 mL of H_2O was added to a solution of 10 mg of HHTP (0.031 mmol) in 1 mL H_2O in a 20 mL scintillation vial, and the mixture was ultrasonicated for 5 min. Then 0.15 mL DMF was then added dropwise followed by 5 min of ultrasonication. This mixture was heated in the vial for 12 hours at 80 °C. The product precipitated out as blue solids. The mixture was centrifuged, decanted and washed with 5 mL deionized water for three times and then 5 mL methanol for another three times and then the solid product was kept in 3 mL methanol.

Samples for powder characterization were prepared by combining the products of multiple synthesis batches prepared as described above, followed by centrifugation, decanting of the liquid and drying at room temperature under weak dry nitrogen flow.

1.2 General characterization
Powder *X*-ray diffraction patterns were recording in θ/2θ Bragg-Brentano geometry using a Bruker Advance II diffractometer equipped with a Ni-filtered CuKα source. The samples were prepared as a thin layer of the powder on a zero-background silicon substrate.

1.3 Adsorptive properties
Adsorption isotherms were collected for powder samples (approx. 35 mg dry weight, pre-activated at 100°C under dynamic vacuum) using a manometric Micromeritics ASAP 2020 gas sorption analyzer. For the N_2 isotherms, Airgas *Ultra High Purity 5.0* grade gases were used for the He free space correction and for the N_2 measurement. Sample temperature control was provided by a liquid nitrogen bath (77 K). The BET surface area analysis was conducted on the 0.005–0.05 P/P_0 range after verification of consistency in this range through the criteria proposed by Rouquerol and co-workers.[5] For the H_2O and CO_2 isotherms the ASAP 2020 instrument was equipped with a vapor dosing option kit, and an isothermal circulation bath for sample temperature control. Airgas CO_2 *Research* grade and deionized water, degassed through multiple freeze-pump-thaw cycles, were used for the measurements. The isotherms at three temperatures (15, 20, 25 °C) were measured in random order using the same sample material re-activated at 100 °C under dynamic vacuum between runs.

For the water adsorption isotherms, a temperature-independent characteristic curve was constructed through concatenated fitting of the three isotherms after transformation of the each measurement pressure to the Polanyi–Adsorption Potential (P_0 = saturation pressure at given temperature, p = pressure):[6,7]

$$U_{polanyi} = RT \ln(\frac{P_0(T)}{p})$$

For the CO_2 adsorption isotherms, the three isotherms were fitted to a Virial type expression (p = pressure, N = amount adsorbed):[8,9]

$$\ln p = lnN + \frac{1}{T}\sum_{i=0}^{m} aN^i + \sum_{i=0}^{n} bN^i$$

The isosteric enthalpies of adsorption ($-Q_{st}$) were calculated through fitting of the slope of the inverse-temperature dependence of the equal surface-coverage pressure of the fitted isotherms, as based on an expression derived from the Clausius–Clapeyron equation:[8]

$$(LnP)_N = \frac{-Q_{st}}{RT} + C$$

1.4 2D MOF IDE chemiresistors

Ohmic behavior of all reported sensors was verified through the linear slopes of the *I-V* traces between −1.5 and 1.5 V, under various conditions analogous to the conductometric experiments.

A wide variation of the initial conductances of the devices was observed, ranging from 0.5 mS to 0.05 nS. The variation is explained by the different bulk electrical conductivities of the tested 2D MOFs, as well as variation of the morphological quality of the deposited layers that were used. The conductance was typically within the same order of magnitude for different devices of the same material, particularly when prepared in the same instance. Optical images of three representative devices of Cu_3HIB_2 prepared in a single instance are shown below.

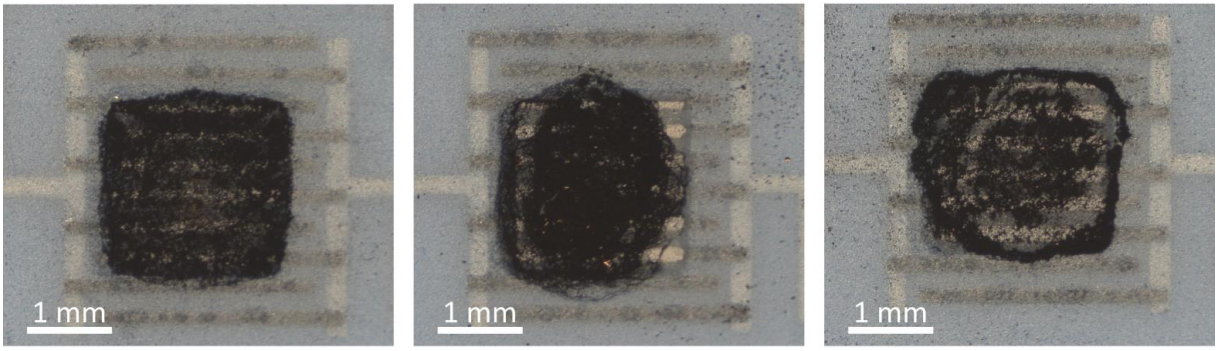

Preliminary to collecting the results reported in this paper, the variation of many device and experimental aspects of the sensing approach were tested (electrode metal, electrode spacing, substrate material, direct current potential, readout current range, *etc*.), and for none of these external factors a significant correlation with the CO_2 response characteristics could be observed.

1.5 Sensor characterization system

A schematic of the home-built sensor characterization setup is shown below.

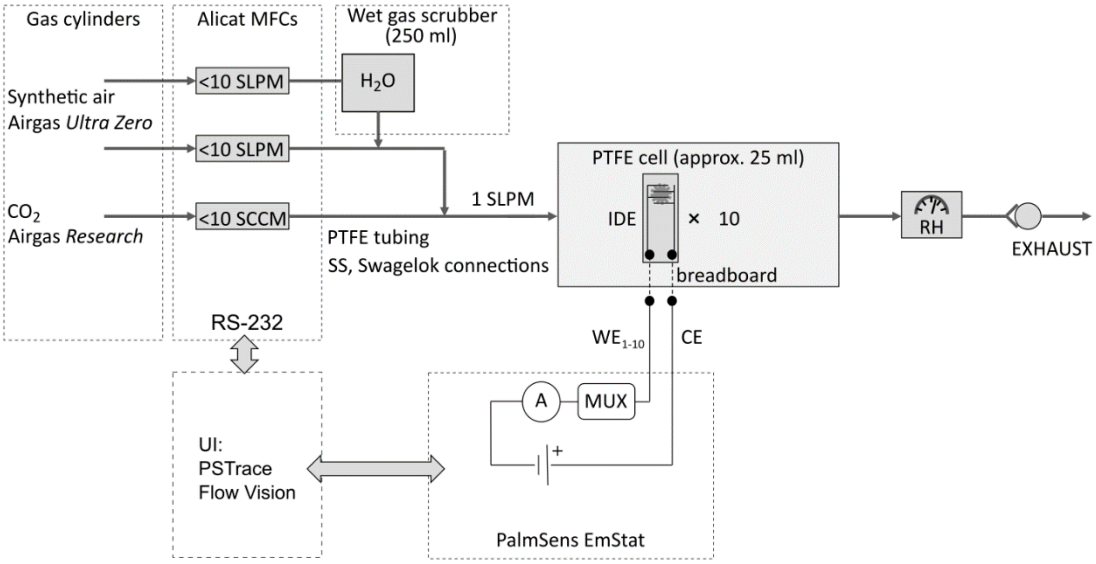

The system was leak-tested throughout the timeline of our study, and accurate operation was verified by measuring the downstream gas composition using a benchtop hygrometer for the relative humidity and a Bruker Tensor 37 FTIR spectrophotometer for CO_2. Linearity of the controlled levels was verified, followed by referencing of at least one concentration with respect to a calibration value (saturated salt solutions for the relative humidity and the ambient level for CO_2).

1.6 Sensing data analysis

The scripted data analysis was conducted using OriginLab OriginPro.

The plotted current-time traces, G/G_0, were 15-point FFT smoothed and normalized by the average current of the time range between 50 and 5 s before the first dosed level. Unless noted otherwise in the caption of the respective figure, no background corrections were applied to the plotted current-time traces. The only exception are the initial runs shown in Figure 1a (chronological order of the initial measurements: 50 %RH, 30 %RH and 70 %RH, respectively), for which minor exponential decaying backgrounds were subtracted to ease the visual comparison. Particularly, the fitted background was anchored to four points of each run (one point before the initial 500 ppm dose of the three repeated units of the sequence, and one point after recovery from the last 2500 ppm dose, respectively).

The quantified responses were calculated directly from the raw measured data, without any additional processing, as follows:
1) G_{DOSE} was calculated as the average current measured for the time range between 50 and 5s before finishing the exposure period of a dosed level;
2) G_{BG} was calculated as the mean of the average currents of the time range between 50 and 5s before starting the exposure period of a dosed level, and the average current of the time range between 50 and 5s before finishing the recovery period of the same dosed level;
3) The response to a dose was calculated as $(G_{DOSE} - G_{BG})(G_{BG})^{-1}$;

4) The mean responses of each device to each level were calculated by repeating steps 1–3 for all doses in the sequence per device, and by subsequent averaging of the values of the repetitive doses;
5) The mean responses (and the standard deviations) of each material to each level were calculated by averaging the mean responses of all devices of the material.

The transient data were extracted through averaging of the background-subtracted current-time traces of 10 devices at each RH. White noise was removed by Loess-filtering. Next, the data was plotted in the form of an integrated first-order rate law:

$$\Delta G(t) = \Delta G_{max}[1 - \exp\left(\frac{-t}{\tau}\right)]$$

1.7 *In situ* diffuse-reflectance spectroscopy
DRIFTS was performed on a Bruker Tensor 37 equipped with a Pike Technologies DiffusIR accessory and with a mercury cadmium telluride detector cooled at 77 K for data collection (16 scans per spectrum). NIR-DRS spectra were collected on a Cary 5000i equipped with a Pike Technologies UV-Vis DiffusIR accessory, data collection was done at 200 nm/min. Our home-built gas mixing system for gas sensor characterization was connected to the inlet of the *in situ* cells and a mineral oil trap was coupled to the outlet. A constant flow of 1 SLPM was provided during all stages of the measurements. The spectra were monitored over time at every new condition of the flow, and a final (steady-state) spectrum was acquired when no temporal changes could be observed for at least 10 minutes.

Absorbance spectra were approximated from the reflectance (R) spectra of the diluted samples through the Kubelka-Munk (K–M) function, F(*R*):

$$\mathrm{F}(R) = \frac{(1-R)^2}{2R}$$

The significant Urbach and deep tailing contributions to the spectrum were excluded from the Tauc fitting range. These contributions can be anticipated at energies lower than the band edge. Notably, fitting of the Urbach tailing ($\alpha \sim \exp(h\nu\, E_U^{-1})$) in the range of 0.6–1 eV did not yield different slopes under the different measured conditions. Therefore no significant changes in the Urbach energy $-E_U-$[10,11] of the sample were observed during exposure to CO_2, consistent with weak charge-trapping interactions affecting the position of the Fermi level, in contrast with breaking of chemical bonds resulting in the formation of strongly bound defect states.

1.8 Computation of band structure and density of states
Beginning with the crystallographic structure presented in a previous publication,[1] the material was geometrically equilibrated using the PBEsol functional, a 500 eV plane wave cutoff, Gamma-centered *k*-grid, and convergence criteria of 10^{-6} eV per formula unit, as implemented in VASP, a commercial software package.[12] A single point HSEsol06 calculation was then used to obtain a better electronic description of the bulk material, and an AFM magnetic orientation was used (Sheet A – spin up; Sheet B – spin down). Spin-orbit coupling was not possible due to memory limitations. The Fermi level was aligned to the Gamma-only Fermi level, and the band structure was plotted using special points mapping to the $C222_1$ space group. Density of states was plotted using a conventional smearing routine for semiconductors.

2. Figures S1–17 and Tables S1–2

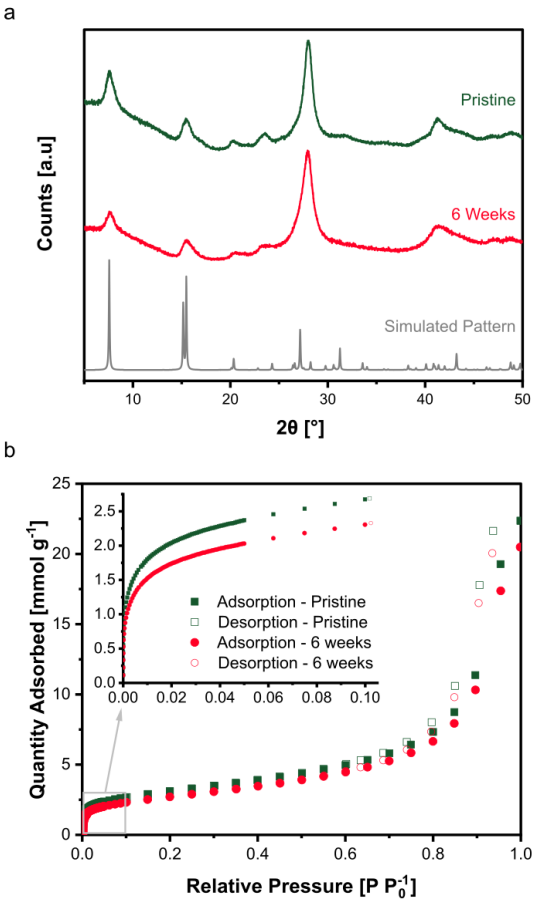

Figure S1. Ambient structural and textural stability of Cu_3HIB_2. A powder sample was synthesized, dried and pretreated analogously to the drop casting procedure used for sensor preparation: a) Powder *X*-ray diffraction patterns of pristine Cu_3HIB_2, the same sample after 6 weeks under ambient atmosphere and the structural model (simulated pattern).; b) Nitrogen adsorption-desorption isotherms at 77 K of the sample at the same two points in time. The Brunauer–Emmett–Teller (BET) surface area evidences preservation of the nanoporous structure, showing an minor drop of 13 % (from 245 m g^{-1}, to 213 m^2 g^{-1}) between the pristine and aged sample. Note that repeated thermal activations and measurements of the water and CO_2 adsorption isotherms were all conducted on the same sample during the 6 week aging period.

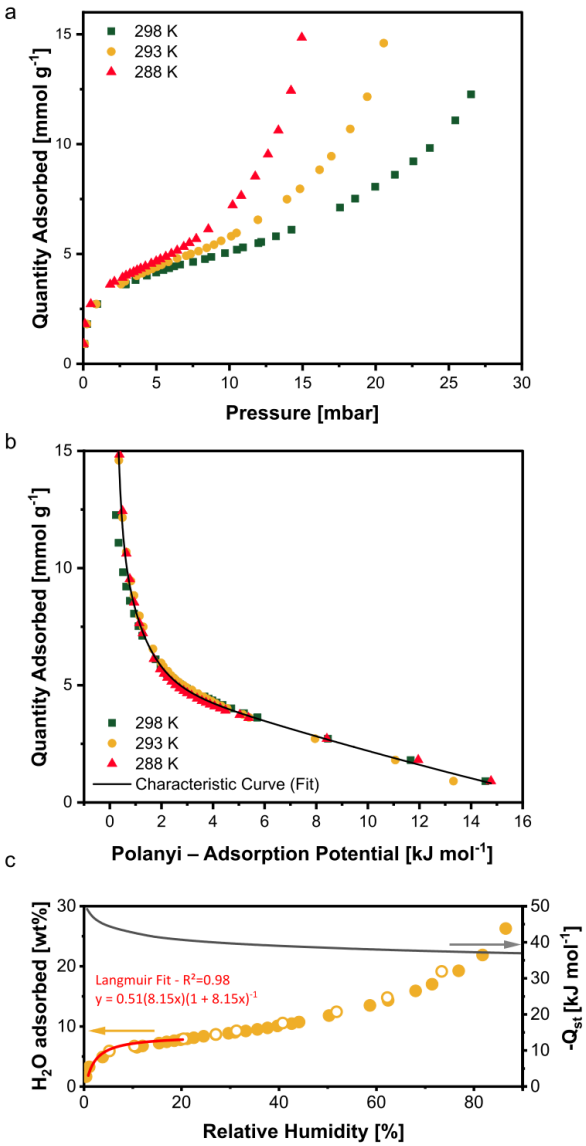

Figure S2. Water adsorption isotherm of Cu_3HIB_2: a) Three isotherms measured on the same sample at 288, 293 and 298 K; b) The isotherms plotted in function of the Polanyi potential, and the concatenated fitted exponential decay function (temperature-independent 'characteristic curve' of the adsorption process).[13] c) Isosteric heat of adsorption ($-Q_{st}$) calculated using the Clausius-Clapeyron equation, plotted in function of the adsorbed amounts of the isotherm at 293 K (closed symbols are the adsorption branch and open symbols the desorption branch of the isotherm). For reference, adsorption of a water molecule at each copper node of the Cu_3HIB_2 framework would correspond to approximately 10.5 wt% H_2O adsorbed based on the chemical formula unit.

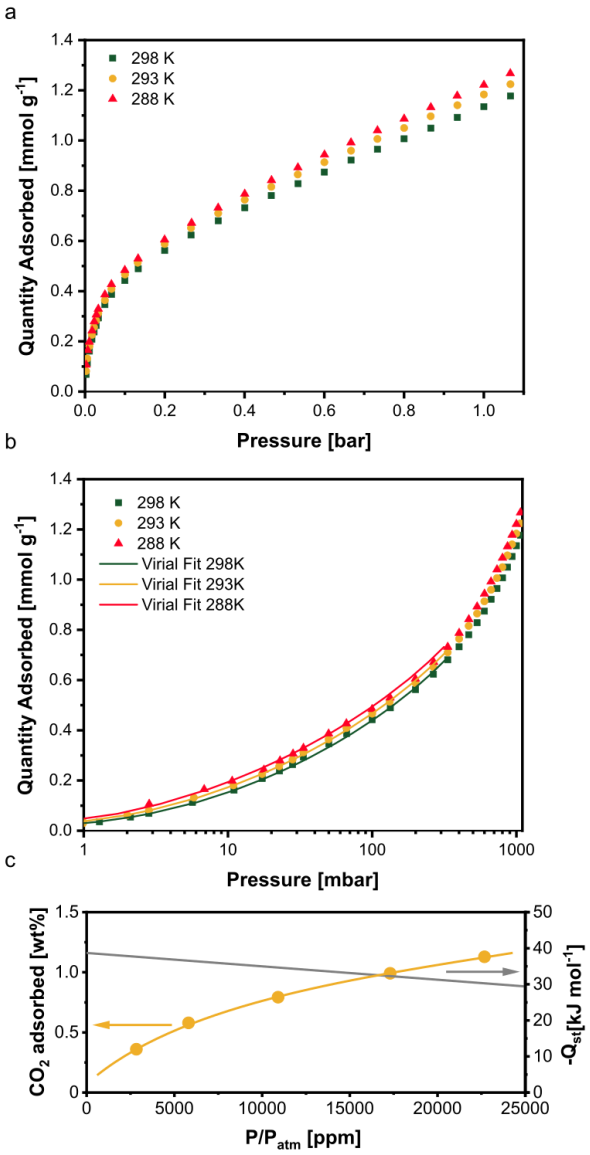

Figure S3. Carbon dioxide adsorption isotherm of Cu_3HIB_2: a) Three isotherms measured on the same sample at 288, 293 and 298 K (for ease of comparison to other works that may plot wt% directly as the measurement unit: the capacity of Cu_3HIB_2 at 1.1 bar and 298 K corresponds to 5.2 wt%); b) Semi-log plot of the virial equation fit at the three measurement temperatures and in pressure range 1–500 mbar; c) Isosteric heat of adsorption (Q_{st}) calculated using the virial equation method,[8] plotted in function of the adsorbed amounts at 293 K. For reference, adsorption of a carbon dioxide molecule at each copper node of the Cu_3HIB_2 framework would correspond to approximately 25.7 wt% CO_2 adsorbed based on the chemical formula unit.

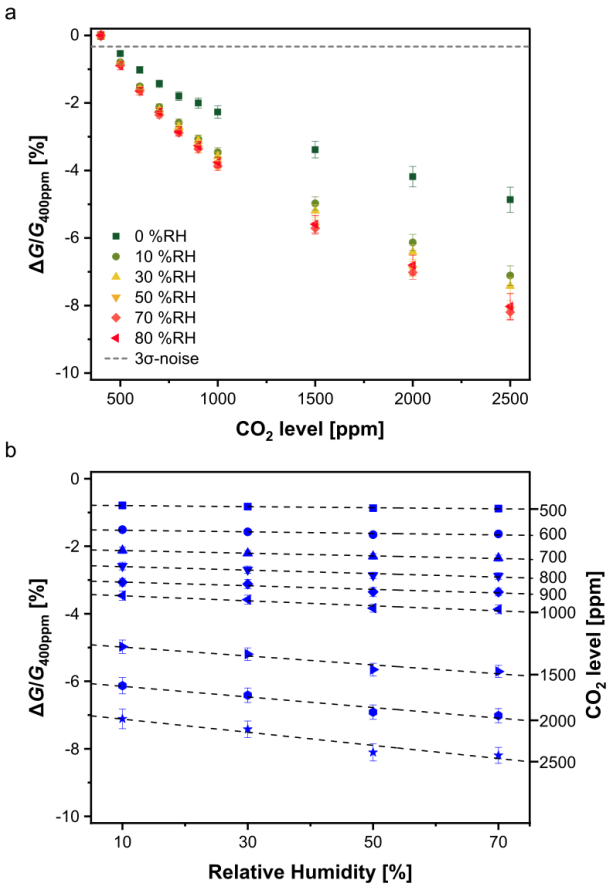

Figure S4. Quantified CO_2 responses of Cu_3HIB_2 in air at room temperature: a) plotted over full measured range between 400 and 2500 ppm (average of 10 devices; supplementary to Fig. **2b** in main paper); b) fitted in function of RH to illustrate the relationship between the response and the CO_2 level for a known or independently measured input of RH. Deviation from linearity (the apparent drop in sensitivity towards higher concentrations) may be attributed to, firstly saturation of the sensor, and secondly underestimation of ΔG (and G_0) at higher levels due to the recorded current not reaching the steady-state value within the 1000s dosing/purging intervals.

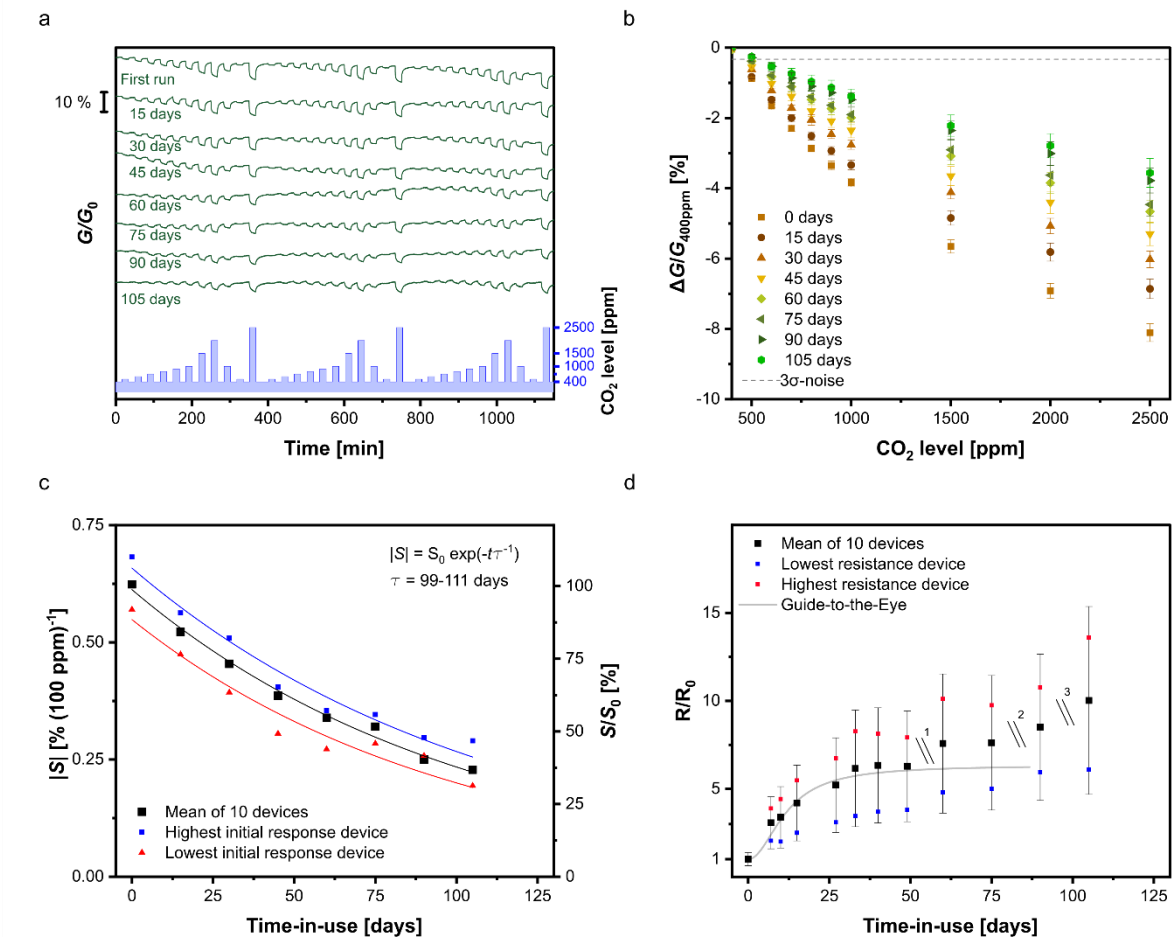

Figure S5. Long-term reliability and stability of Cu_3HIB_2 sensors: a) Current-time traces (vertically offset for clarity) of one representative device subjected to the same test conditions at different points in time over 3.5 months; b) Quantified CO_2 responses of each experiment (average responses and one standard deviation of 10 devices); c) Time-dependence of the sensitivity *S* in the 400–1000 ppm range: mean of the 10 devices and the initially most/least sensitive devices of the set. The lines are fits of the exponential decay function as indicated in the top-right corner of the graph ; d) Time-dependence of the resistance of the 10 devices normalized to the initial value (average and one standard deviation), and of the initially lowest/highest resistance devices. During the breaks indicated on the graph in panel d, the devices were dismounted from the measurement cell and stored on the bench in a closed Gel-Pack®. In between all measurements, the devices were stored open to ambient conditions (ambient air, natural indoor RH fluctuations of approx. 30–55 %, fluctuations of day light and artificial light, 20–22 °C temperature fluctuations).

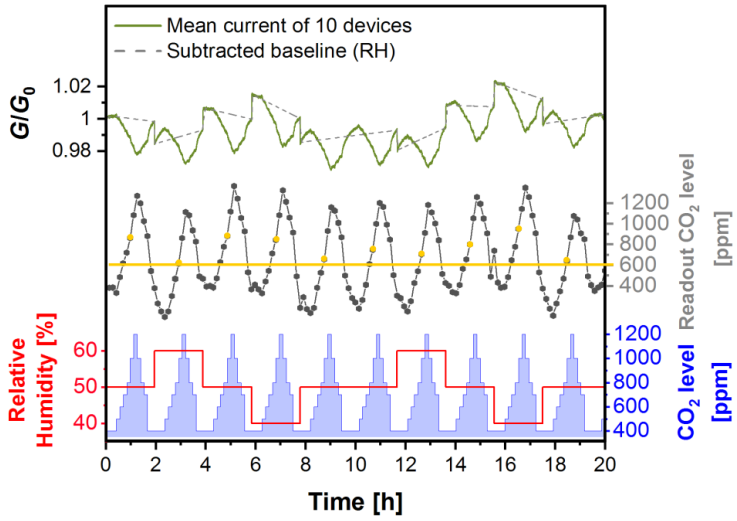

Figure S6. Simulated 'real-world' operation after three months, under simulated conditions of changing RH and CO_2. Plotted are: the mean current-time trace (green full line) of 10 device subjected in parallel to identical test conditions, the subtracted RH background trace based on the currents reached just before and just after switching the RH to a new level (gray dashed line), and the sensor readout level for 100s intervals (grey connected dots), calculated by multiplying the RH baseline corrected G/G_0 by S = –0.25 % (100 ppm)$^{-1}$, which is the sensitivity at 50 %RH extracted from Figure S6 after 90 days. The red and blue traces in the bottom of the plot show the simulated test conditions of CO_2 and RH: 100–200 ppm increments for 100–200 s, and levels between 400 and 1200 ppm, cycled at different RH between 40 and 60 %. This practical 'proof-of-concept' experiment illustrates the capability and robustness of the sensors as operation of the sensors is analytical even after three months and with a simple correction for the RH cross-selectivity. The yellow line and dots highlight the readout values 200 s after switching from 600 to 700–800 ppm. Analogous detection of a threshold level increase (or decrease) is applicable in demand-controlled ventilation of buildings.

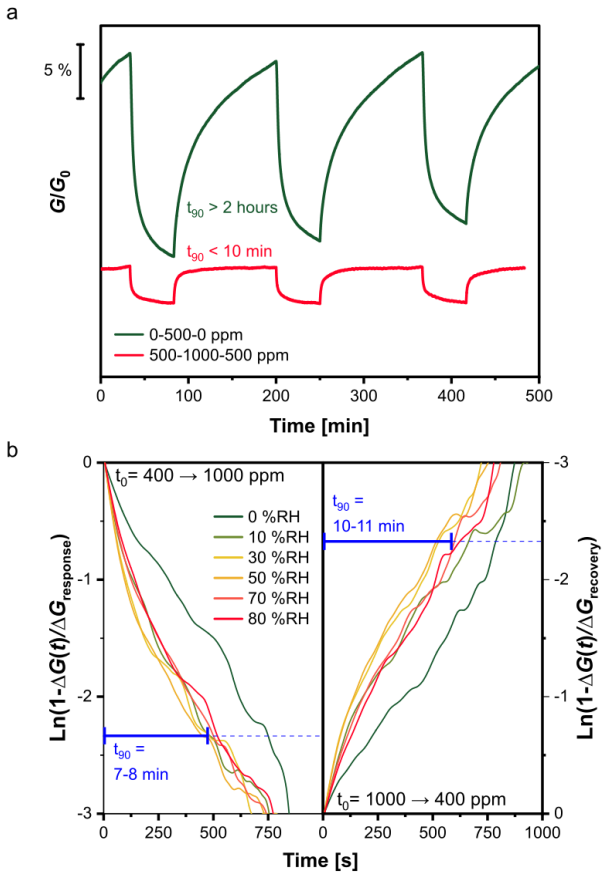

Figure S7. Dependence of kinetics of Cu_3HIB_2 CO_2 sensing on background level of CO_2 and RH:. a) Current-time traces (vertically offset for clarity) for CO_2 level variations in air and at room temperature and 50 %RH, from 0 to 500 and 500 to 1000 ppm, and the corresponding decreases from 500 to 0 and 1000 to 500 ppm (average signal of 10 devices); b) Normalized response-recovery curves after instant carbon dioxide level increase from 400 to 1000 ppm, and the corresponding decrease from 1000 to 400 ppm (noise-filtered average of 10 devices at each RH).

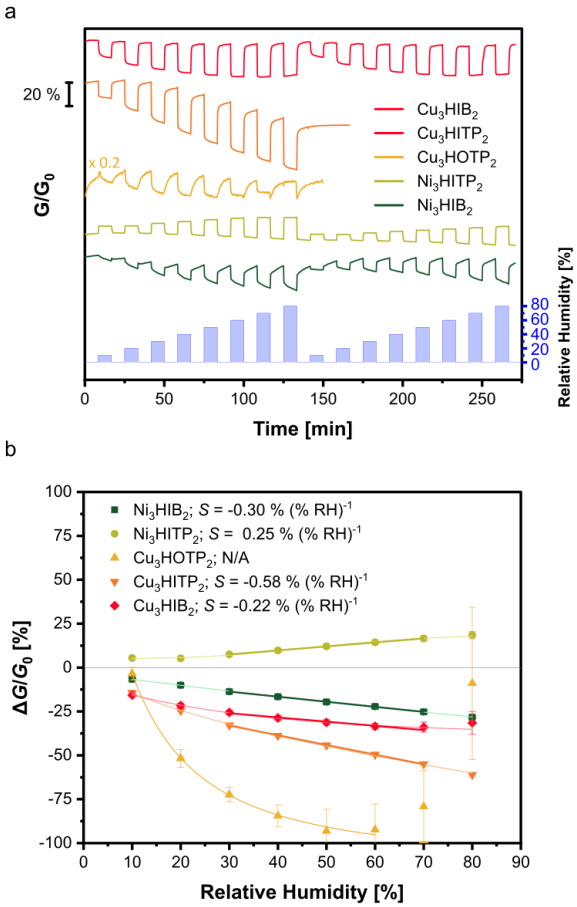

Figure S8. Screening of RH sensing properties and related 2D MOF materials in air at room temperature. a) Current-time traces (vertically offset for clarity) of one representative device of each tested material. Humid air was sequentially dosed (10–80 %RH) using 500s intervals of dosing and purging. Note that the chemiresistive responses of Cu_3HOTP_2 and Cu_3HITP_2 were overshadowed by irreversible increases in the resistance of the devices; b) Quantified responses of the experiments (average responses and standard deviation of 5 devices in function of the dosed concentrations). Sensitivities to RH variations were calculated from the linear interpolation in the 30–70 %RH range.

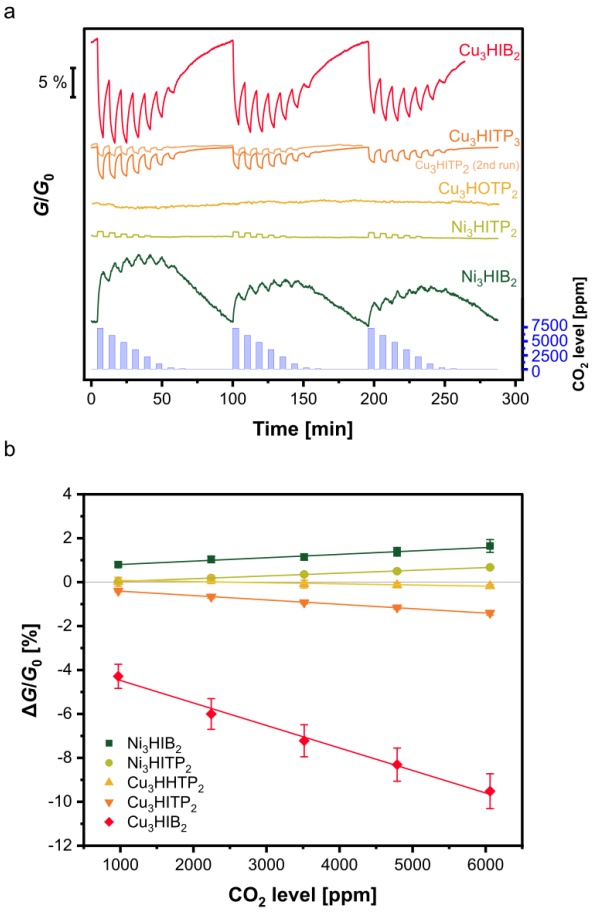

Figure S9. Screening of carbon dioxide sensing properties of Cu_3HIB_2 and related 2D MOF materials in 0–7500 ppm concentration range, in dry air and at room temperature. a) Current-time traces (vertically offset and linear baseline corrected for clarity) of one representative device of each tested material. Carbon dioxide was sequentially dosed from 0 to 300–7500 ppm levels, using 250s intervals of dosing and purging. A second run was measured for Cu_3HITP_2, to confirm the substantial degradation of the response that was observed beyond the time scale of the first run. b) Quantified responses of the experiments (average responses and standard deviations of 5 devices of each material in function of the dosed concentrations). For the Cu_3HITP_2 material, a fast decay of the response was observed and only the lower , practically relevant (*pseudo*-stable) responses observed during the second run were taken into account in the quantification. Notably, for the narrower pore materials (Cu/Ni_3HIB_2) the currents reached after 250s purging and dosing times provided only rough approximations of G_0 and ΔG, due to the slow kinetics of reaching steady state (equilibrium) after switching from 0 to high levels (and reverse). Nevertheless, during these initial screening experiments we used the extracted responses to extrapolate the potential performance of the materials for practical sensing of carbon dioxide at levels in the range of 1000–2000 ppm. These responses clearly demonstrate the superior signal resolution and dynamic range of Cu_3HIB_2 relative to the other related 2D MOF materials that were tested.

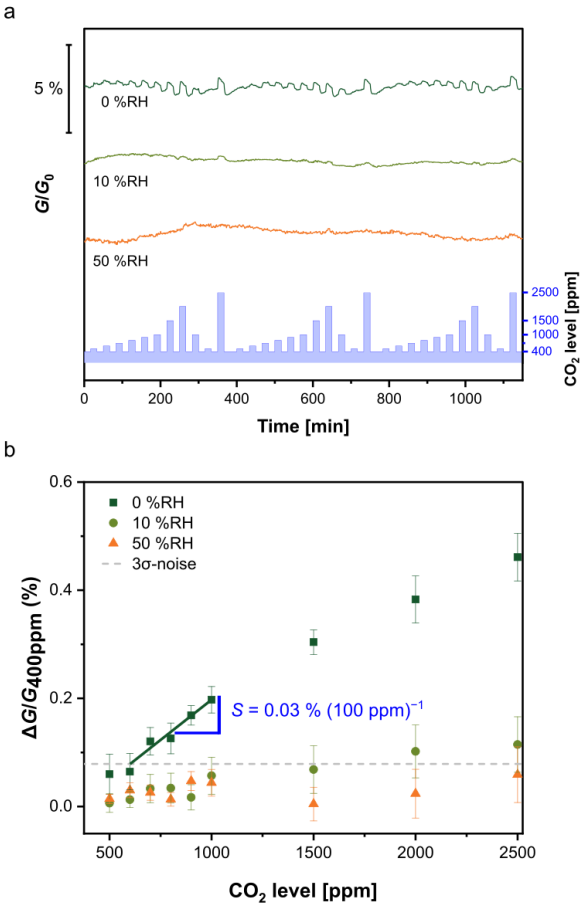

Figure S10. Ambient carbon dioxide sensing properties of Ni_3HIB_2 at levels between 400 and 2500 ppm at room temperature in air. a) Current-time traces (vertically offset for clarity) of one representative device tested at different RH. Carbon dioxide was sequentially dosed at 400–2500 ppm levels using 1000s intervals of dosing and purging. For clarity a polynomial baseline correction was applied in plotting of these experiment; b**)** Quantified responses of the experiment (average responses and standard deviation of 10 devices in function of the dosed concentrations).

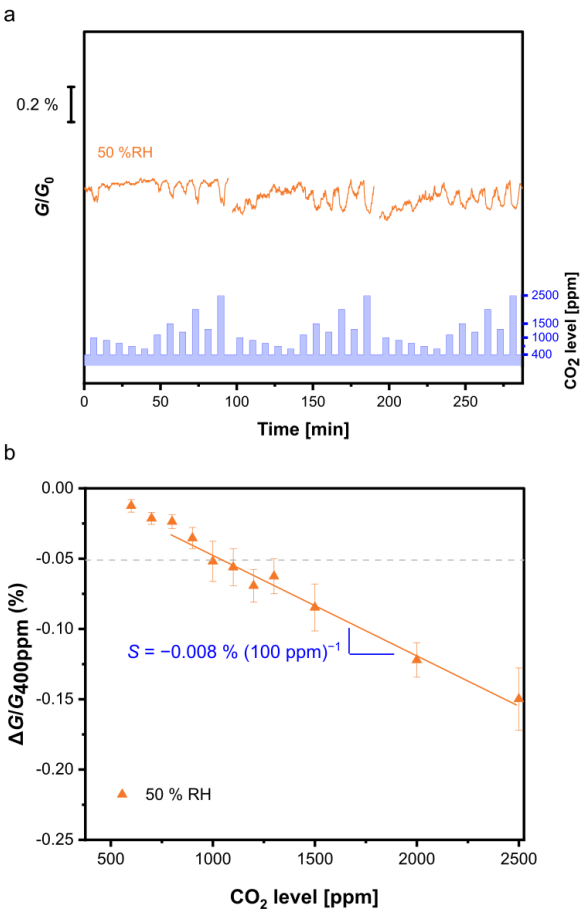

Figure S11. Ambient carbon dioxide sensing properties of Ni_3HITP_2 at levels between 400 and 2500 ppm at room temperature in air. a) Current-time traces of one representative device tested at 50 %RH. Carbon dioxide was sequentially dosed at 400–2500 ppm levels using 250s intervals of dosing and purging. b**)** Quantified responses of the experiment (average responses and standard deviation of 10 devices in function of the dosed concentrations).

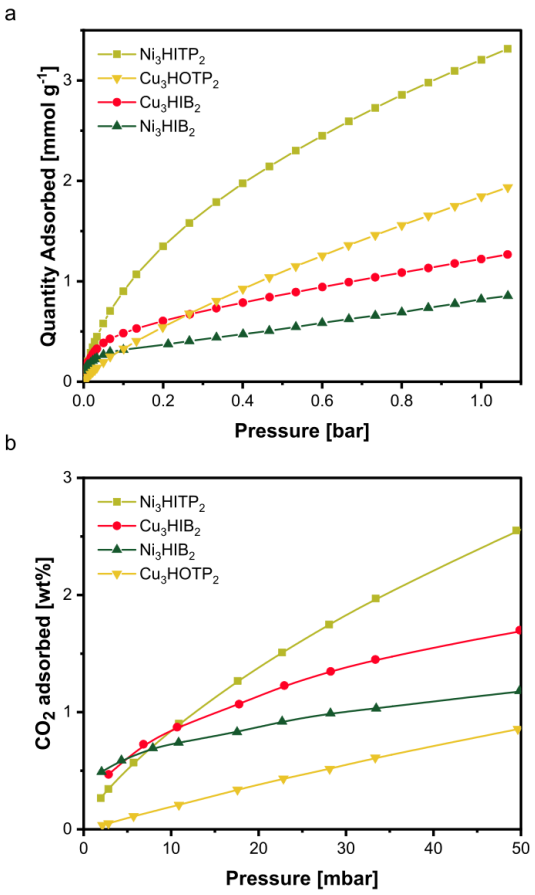

Figure S12. CO_2 adsorption isotherms at 288 K of Ni_3HITP_2, Cu_3HOTP_2, Cu_3HIB_2 and Ni_3HIB_2: a) Full-range plots; b) Plots of the lower pressure range. The steep uptake in the low end of the pressure range (0.5–1 wt% below 10 mbar) can be assigned to interactions with the imino-semiquinonate moieties of these three materials; by contrast, this moiety is not present in the Cu_3HOTP_2 material. The uptake at higher pressures is anticipated to scale with the accessible porosity and surface areas of the materials, which are higher for the larger pore analogs. The uptake at lower pressures is anticipated to scale with the numeric density of NH moieties, which can be simply estimated using the reported crystallographic structures: 20 NH $(nm)^{-3}$ for M_3HIB_2, and 8.8 NH $(nm)^{-3}$ for M_3HITP_2, respectively.

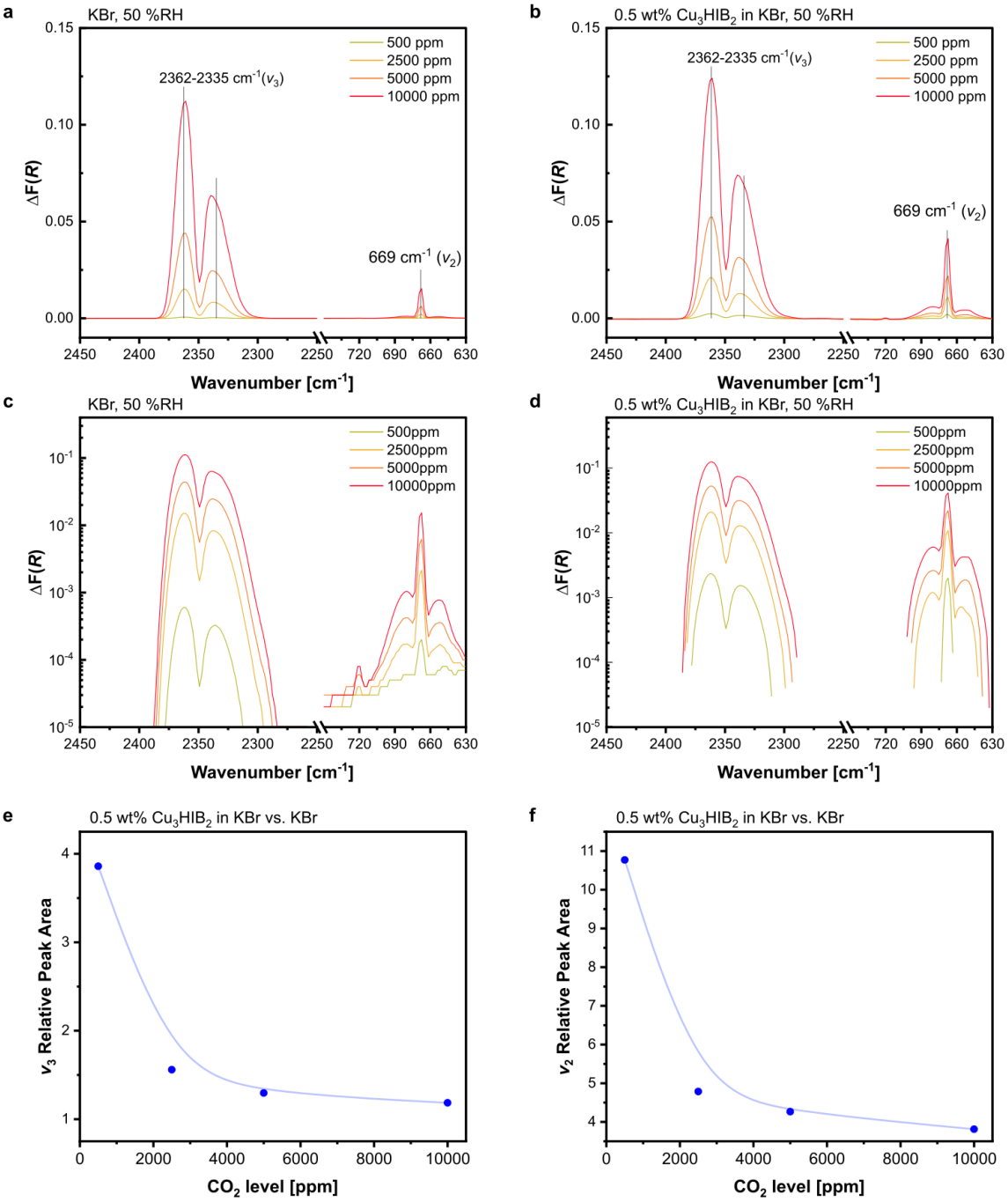

Figure S13. Detailed comparison of the carbon dioxide vibrational bands in function of concentration for the *in situ* DRIFTS spectra acquired in air at 50 %RH. a) KBr reference sample; b) Cu_3HIB_2 sample in KBr; c) KBr reference sample, semi-log plot; d) Cu_3HIB_2 sample in KBr, semi-log plot; e) Relative peak area of the carbon dioxide v_3 mode; f) Relative peak area of the carbon dioxide v_2 mode. Qualitative comparison indicates adsorptive accumulation of CO_2 by Cu_3HIB_2, particularly at low CO_2 levels.

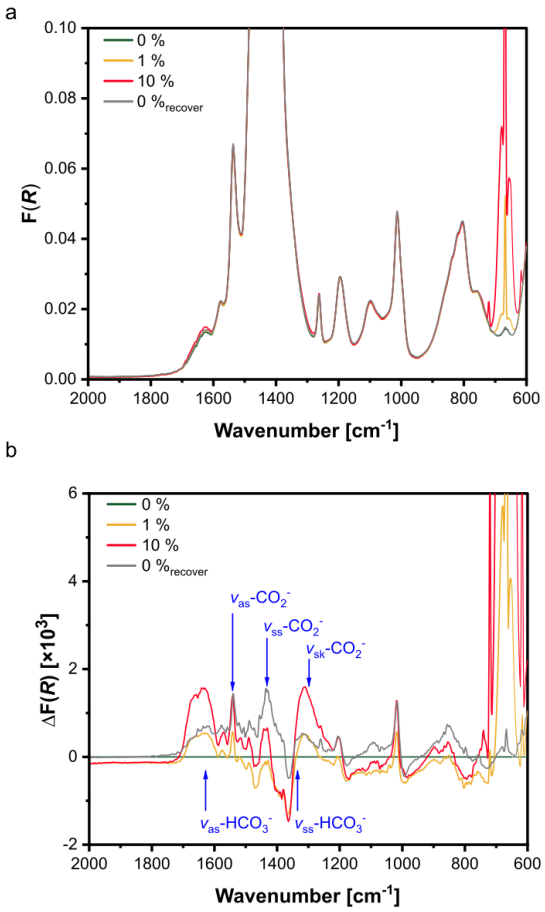

Figure S14. *In situ* DRIFTS spectra acquired in air at 10 %RH, and 0–10 % CO_2 levels. a) Kubelka-Munk transformed spectra; b) Difference spectra obtained by subtracting the initial spectrum (0 % CO_2) from the subsequently acquired spectra. Peak assignments in the difference spectra are based on reported bands of silica-supported sterically hindered amines at similar levels of CO_2 and RH.[14] Although convoluted due to the ligand vibrational bands, bicarbonate and carbamate stretching modes (*ss: symmetric stretch; as: asymmetric stretch; sk: skeletal stretch*) can be found in correlation with the increasing CO_2 level. Presumably due to the low abundance of these species, no observations could be made at lower concentrations. Moreover, to observed spectral changes at high levels of CO_2 appear only semi-reversible, particularly in the case of the presumed carbamate modes. The mode at 1014 cm^{-1} showing an irreversible increase in intensity, is presumed to be the ligand CN stretching mode. It is currently unclear why this particular mode is affected to by exposure to high levels of CO_2.

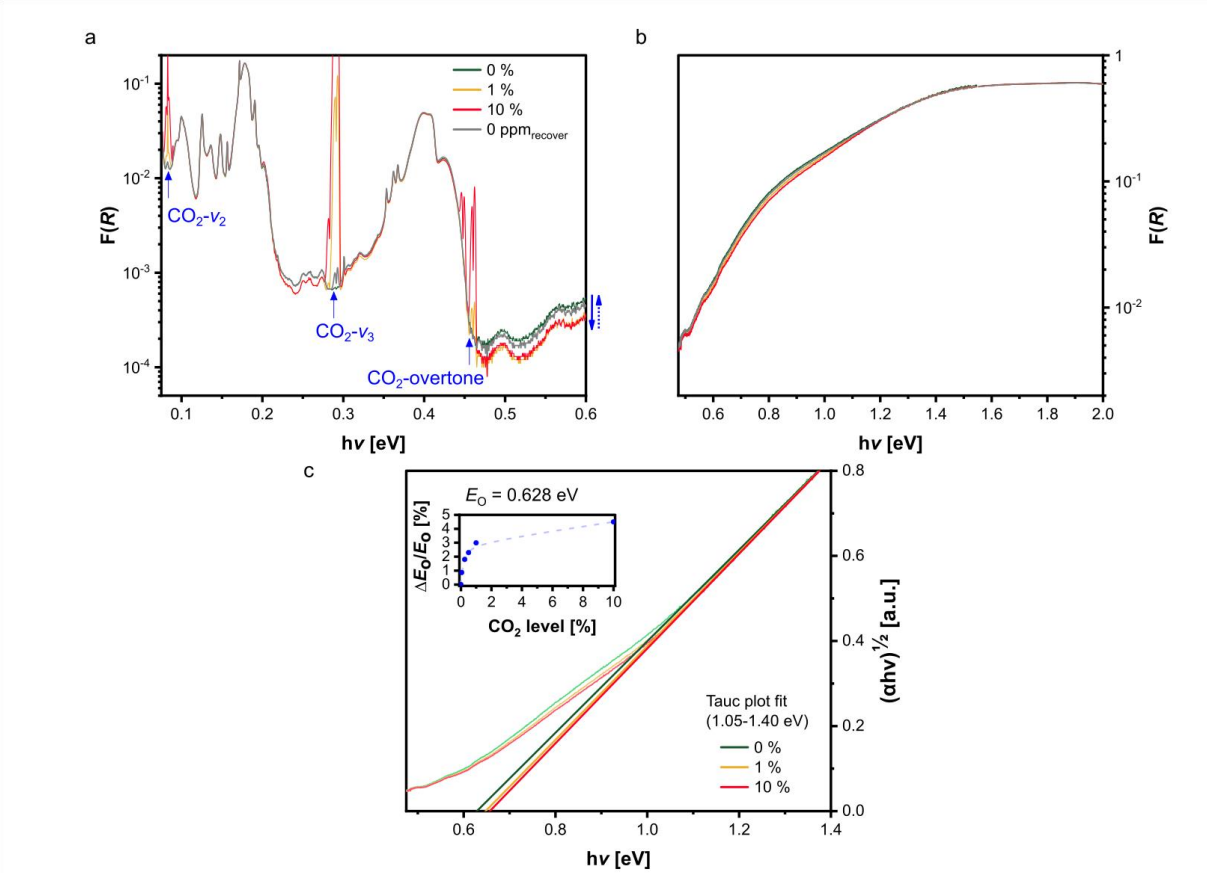

Figure S15. *In situ* spectroscopic probing of the origin of the Cu_3HIB_2 chemiresistive response under air at 10 %RH and CO_2 levels between 0 and 10 %. a) Kubelka-Munk transformed DRIFTS; b) Kubelka-Munk transformed DRS-NIR; c) The Tauc plot indicates a reversible widening of the band gap upon adsorption of carbon dioxide in humid Cu_3HIB_2. This experiments shows a slightly decreased effect at lower RH (in comparison to the data obtained at 50%RH in the article), and confirms the saturation of the effect towards higher concentrations. For clarity only the far ends of the measured range are shown here (0 and 1% CO_2), as the other levels showed a similar trend to the spectra shown in the main paper, as can be seen from the extrapolated band gaps in the inset of panel c.

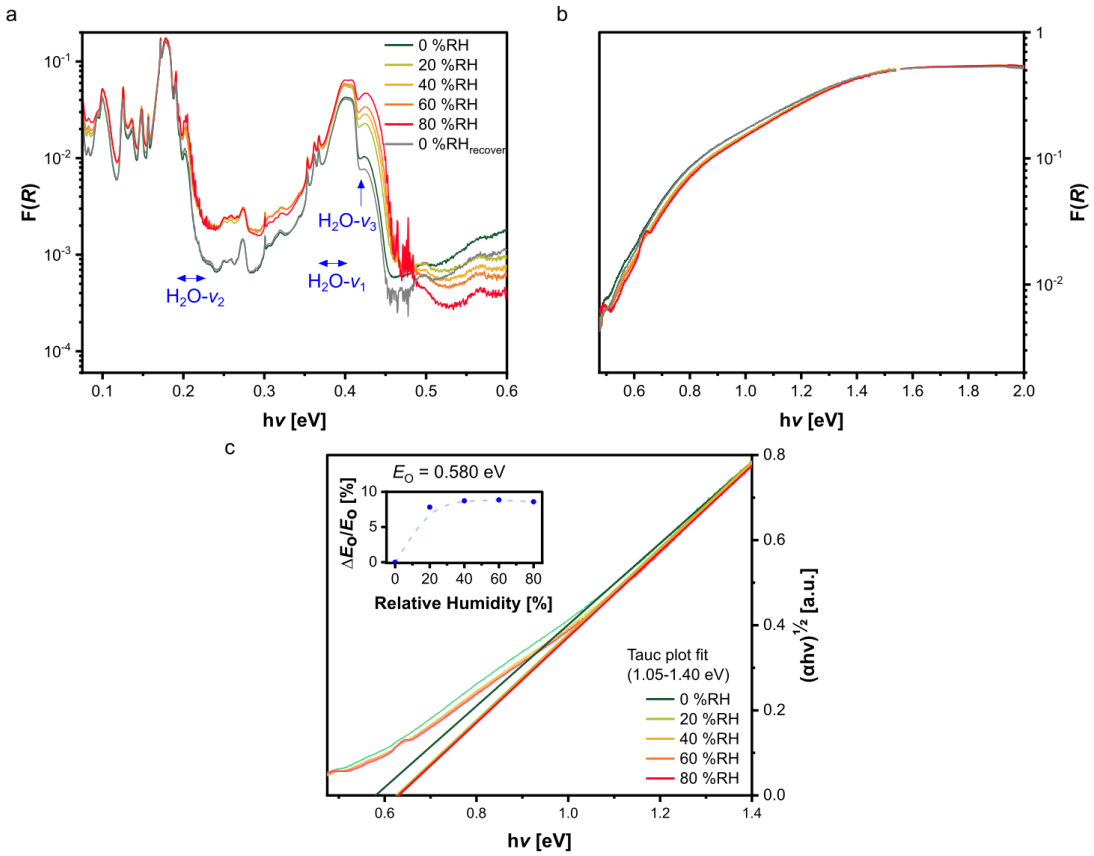

Figure S16. *In situ* spectroscopic probing of the origin of the Cu_3HIB_2 chemiresistive response under air between 0 and 80 %RH. a) Kubelka-Munk transformed DRIFTS; b) Kubelka-Munk transformed DRS-NIR; c) The Tauc plot indicates a reversible widening of the band gap upon adsorption of water in Cu_3HIB_2. This experiments confirms the contribution of water to the widening of the band gap. The effect of water shows saturation between 0 and 20 %RH, consistent with filling of the pores in this range.

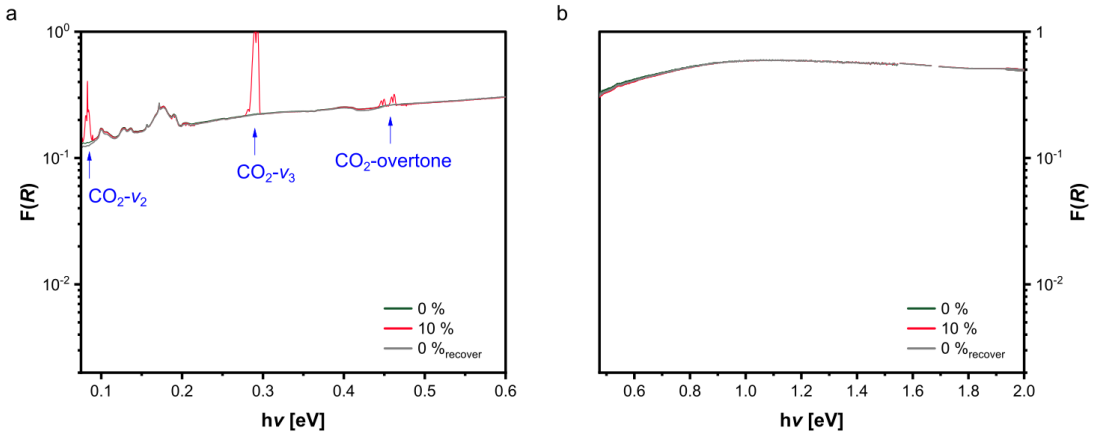

Figure S17. *In situ* spectroscopic probing of the origin of the Ni_3HIB_2 chemiresistive response under air at 50 %RH and CO_2 levels between 0 and 10 %. a) Kubelka-Munk transformed DRIFTS; b) Kubelka-Munk transformed DRS-NIR. The data is plotted using the same axis scales as used for the analogous experiments with Cu_3HIB_2. No significant changes were observed in the NIR range upon dosing with carbon dioxide.

Table S1: Overview of demonstrated metal-organic framework CO_2 sensors

Material	**Transduction approach**	**Tested conditions**	**Tested range**	**LOD*[1]**	**Source**
Cu_3HIB_2	Chemiresistor	air, 0–80 %RH	400–2500 ppm	Baseline +67 ppm	This work
ZIF-8	SAW	N_2, 0 %RH	0–100 %	10 000 ppm	[15]
ZIF-8	QCM	N_2, 0 %RH	0–100 %	50 000 ppm	[15]
ZIF-8	Optical waveguide	N_2, 0-75 %RH	0–100 %	3000 ppm	[16]
CD-MOF	EIS	N_2, 0 %RH	0–100 %	<1–5 %	[17]
CD-MOF	Chemiresistor	ambient air vs. 100 % CO_2	100 %	*N/A*	[18]
(ED/)MOF-74	Kelvin probe	air, 0–50 %RH	400–5000 ppm	Baseline +600 ppm	[19]
MIL-53/CB or CNT	Chemiresistor	Vacuum, 0-20 bar CO_2	100 %	*N/A*	[20]

*[1]LOD = limit-of-detection (lowest measurable increase from baseline concentration); as reported (experimental limit or S/N extrapolation), or estimate based on the reported data.

Table S2: Overview of demonstrated room temperature solid-state electronic CO_2 sensors*[1]

Material	**Tested conditions**	**Tested range [ppm]**	**|S| [% (100 ppm)$^{-1}$] *[2]**	**Kinetics, t_{90} (response, recovery)**	**Stability/reliability (demonstrated by data)**	**Reference**
Cu_3HIB_2	air, 0-80 %RH	400-2500	0.6-0.4 (80–0 %RH)	7 min, 10 min	> 3 months (τ = 99–111 days)	This work
Ni_3HIB_2	air, 0-50 %RH	400-2500	$<10^{-3}$ (50 %RH) 3.0×10^{-2} (0 % RH)	minute-range	> 1–2 days	This work
Ni_3HITP_2	air, 0-50 %RH	400-2500	8×10^{-3} (50 % RH) 2×10^{-2} (0 % RH)	second-range	> 1–2 days	This work
PEI/PANI	air, 10-50 %RH	0-5000	0.6 (50 %RH) 0.2 (35 %RH) <LOD (10 %RH)	7 min, 10 min	/	21
PANI	air, 35 %RH	0-5000	0	/	/	21
PEI/PEDOT	N_2, 15-95 %RH	0-1000	0.2 (80 %RH) 3×10^{-2} (55 %RH) <LOD (16 %RH)	30 min, 1 hour	> 1 day (~30% drop)	22
PEI/starch/CNT	air, 80 %RH	500-100000	0.2	<1 min, <2 min	/	23
rGO	air, 0 %RH	0-7000	2×10^{-2}	minute-range	/	24
rGO	air, 68 %RH	350-1500	1.3	4 min, 4 min	/	25
PEI/rGO	N_2, 0 %RH	0-15000	8×10^{-2}	10 min, 10 min	/	26
Graphene	various, <1 %RH	0-2000	9×10^{-4}	second-range	/	27
Graphene/ PEDOT-PSS	ambient air	400-1400	2×10^{-2}	/	/	28
$La_2O_2CO_3$-NP/PIL	air, 50 %RH	150-2400	0.15	minute-range	> 4 days	29
Al_2O_3-NP/PIL	air, 30-70 %RH	150-3000	0.1 (30–50 %RH) 5×10^{-2} (60–70 %RH)	<5 min,<45 min	> 1 week	30

*[1]Selected publications from a broad literature search using the following selection criteria: solid-state sensors, direct-electronic signal transduction (*i.e.* impedance/resistance modulation of sensing material), (near-)room temperature operation, studies reporting device performance in 500-1000 ppm range or wider. For similar and incremental works, only the highest demonstrated sensitivities are included. For clear comparison, all reported results were converted to the form $\Delta X/X_{bg}$, $\Delta X = X_{CD} - X_{bg}$ (X = G,R and bg and CD referring to the steady-state recorded value after purging with the purge gas and the background level of CO_2, respectively dosing with increased levels of CO_2). *[2]Reported value or by calculation of the slope in the range 500–1000 ppm of the reported response behavior (LOD = limit-of-detection).

3. References

(1) Dou, J.-H.; Sun, L.; Ge, Y.; Li, W.; Hendon, C. H.; Li, J.; Gul, S.; Yano, J.; Stach, E. A.; Dincă, M. Signature of Metallic Behavior in the Metal–Organic Frameworks M3(Hexaiminobenzene)2 (M = Ni, Cu). *J. Am. Chem. Soc.* **2017**, *139* (39), 13608–13611. https://doi.org/10.1021/jacs.7b07234.

(2) Campbell, M. G.; Sheberla, D.; Liu, S. F.; Swager, T. M.; Dincă, M. Cu_3(Hexaiminotriphenylene)$_2$: An Electrically Conductive 2D Metal-Organic Framework for Chemiresistive Sensing. *Angew. Chem. Int. Ed.* **2015**, *54* (14), 4349–4352. https://doi.org/10.1002/anie.201411854.

(3) Sheberla, D.; Sun, L.; Blood-Forsythe, M. A.; Er, S.; Wade, C. R.; Brozek, C. K.; Aspuru-Guzik, A.; Dincă, M. High Electrical Conductivity in Ni3(2,3,6,7,10,11-Hexaiminotriphenylene)2, a Semiconducting Metal-Organic Graphene Analogue. *J. Am. Chem. Soc.* **2014**, *136* (25), 8859–8862. https://doi.org/10.1021/ja502765n.

(4) Hmadeh, M.; Lu, Z.; Liu, Z.; Gandara, F.; Furukawa, H.; Wan, S.; Augustyn, V.; Chang, R.; Liao, L.; Zhou, F.; et al. New Porous Crystals of Extended Metal-Catecholates. *Chem. Mater.* **2012**, *24* (18), 3511–3513. https://doi.org/10.1021/cm301194a.

(5) Rouquerol, J.; Llewellyn, P.; Rouquerol, F. Is the BET Equation Applicable to Microporous Adsorbents? *Stud. Surf. Sci. Catal.* **2007**, *160*, 49–56.

(6) de Lange, M. F.; van Velzen, B. L.; Ottevanger, C. P.; Verouden, K. J. F. M.; Lin, L.-C.; Vlugt, T. J. H.; Gascon, J.; Kapteijn, F. Metal–Organic Frameworks in Adsorption-Driven Heat Pumps: The Potential of Alcohols as Working Fluids. *Langmuir* **2015**, *31* (46), 12783–12796. https://doi.org/10.1021/acs.langmuir.5b03272.

(7) Rieth, A. J.; Yang, S.; Wang, E. N.; Dincă, M. Record Atmospheric Fresh Water Capture and Heat Transfer with a Material Operating at the Water Uptake Reversibility Limit. *ACS Cent. Sci.* **2017**, *3* (6), 668–672. https://doi.org/10.1021/acscentsci.7b00186.

(8) Sumida, K.; Rogow, D. L.; Mason, J. A.; McDonald, T. M.; Bloch, E. D.; Herm, Z. R.; Bae, T.-H.; Long, J. R. Carbon Dioxide Capture in Metal-Organic Frameworks. *Chem. Rev.* **2012**, *112* (2), 724–781. https://doi.org/10.1021/cr2003272.

(9) Wright, A. M.; Wu, Z.; Zhang, G.; Mancuso, J. L.; Comito, R. J.; Day, R. W.; Hendon, C. H.; Miller, J. T.; Dincă, M. A Structural Mimic of Carbonic Anhydrase in a Metal-Organic Framework. *Chem* **2018**, *4* (12), 2894–2901. https://doi.org/10.1016/j.chempr.2018.09.011.

(10) Kurik, M. V. Urbach Rule. *Phys. Status Solidi A* **1971**, *8* (1), 9–45. https://doi.org/10.1002/pssa.2210080102.

(11) Singh, J.; Shimakawa, K. *Advances in Amorphous Semiconductors*; Advances in condensed matter science; Taylor & Francis: London ; New York, 2003.

(12) Kresse, G.; Furthmüller, J. Efficient Iterative Schemes for Ab Initio Total-Energy Calculations Using a Plane-Wave Basis Set. *Phys. Rev. B* **1996**, *54* (16), 11169.

(13) Dubinin, Mm. The Potential Theory of Adsorption of Gases and Vapors for Adsorbents with Energetically Nonuniform Surfaces. *Chem. Rev.* **1960**, *60* (2), 235–241.

(14) Lee, J. J.; Yoo, C.-J.; Chen, C.-H.; Hayes, S. E.; Sievers, C.; Jones, C. W. Silica-Supported Sterically Hindered Amines for CO_2 Capture. *Langmuir* **2018**, *34* (41), 12279–12292. https://doi.org/10.1021/acs.langmuir.8b02472.

(15) Devkota, J.; Kim, K.-J.; Ohodnicki, P. R.; Culp, J. T.; Greve, D. W.; Lekse, J. W. Zeolitic Imidazolate Framework-Coated Acoustic Sensors for Room Temperature Detection of Carbon Dioxide and Methane. *Nanoscale* **2018**, *10* (17), 8075–8087. https://doi.org/10.1039/C7NR09536H.

(16) Chocarro-Ruiz, B.; Pérez-Carvajal, J.; Avci, C.; Calvo-Lozano, O.; Alonso, M. I.; Maspoch, D.; Lechuga, L. M. A CO_2 Optical Sensor Based on Self-Assembled Metal–organic Framework Nanoparticles. *J. Mater. Chem. A* **2018**, *6* (27), 13171–13177. https://doi.org/10.1039/C8TA02767F.

(17) Gassensmith, J. J.; Kim, J. Y.; Holcroft, J. M.; Farha, O. K.; Stoddart, J. F.; Hupp, J. T.; Jeong, N. C. A Metal–Organic Framework-Based Material for Electrochemical Sensing of Carbon Dioxide. *J. Am. Chem. Soc.* **2014**, *136* (23), 8277–8282. https://doi.org/10.1021/ja5006465.

(18) Shen, D.; Wang, G.; Liu, Z.; Li, P.; Cai, K.; Cheng, C.; Shi, Y.; Han, J.-M.; Kung, C.-W.; Gong, X.; et al. Epitaxial Growth of γ-Cyclodextrin-Containing Metal–Organic Frameworks Based on a Host–Guest Strategy. *J. Am. Chem. Soc.* **2018**, *140* (36), 11402–11407. https://doi.org/10.1021/jacs.8b06609.

(19) Pentyala, V.; Davydovskaya, P.; Ade, M.; Pohle, R.; Urban, G. Carbon Dioxide Gas Detection by Open Metal Site Metal Organic Frameworks and Surface Functionalized Metal Organic Frameworks. *Sens. Actuators B Chem.* **2016**, *225*, 363–368. https://doi.org/10.1016/j.snb.2015.11.071.

(20) Freund, P.; Mielewczyk, L.; Rauche, M.; Senkovska, I.; Ehrling, S.; Brunner, E.; Kaskel, S. MIL-53(Al)/Carbon Films for CO_2 -Sensing at High Pressure. *ACS Sustain. Chem. Eng.* **2019**, *7* (4), 4012–4018. https://doi.org/10.1021/acssuschemeng.8b05368.

(21) Srinives, S.; Sarkar, T.; Hernandez, R.; Mulchandani, A. A Miniature Chemiresistor Sensor for Carbon Dioxide. *Anal. Chim. Acta* **2015**, *874*, 54–58. https://doi.org/10.1016/j.aca.2015.03.020.

(22) Chiang, C.-J.; Tsai, K.-T.; Lee, Y.-H.; Lin, H.-W.; Yang, Y.-L.; Shih, C.-C.; Lin, C.-Y.; Jeng, H.-A.; Weng, Y.-H.; Cheng, Y.-Y.; et al. In Situ Fabrication of Conducting Polymer Composite Film as a Chemical Resistive CO2 Gas Sensor. *Microelectron. Eng.* **2013**, *111*, 409–415. https://doi.org/10.1016/j.mee.2013.04.014.

(23) Star, A.; Han, T.-R.; Joshi, V.; Gabriel, J.-C. P.; Grüner, G. Nanoelectronic Carbon Dioxide Sensors. *Adv. Mater.* **2004**, *16* (22), 2049–2052. https://doi.org/10.1002/adma.200400322.

(24) Zhou, Y.; Jiang, Y.; Xie, T.; Tai, H.; Xie, G. A Novel Sensing Mechanism for Resistive Gas Sensors Based on Layered Reduced Graphene Oxide Thin Films at Room Temperature. *Sens. Actuators B Chem.* **2014**, *203*, 135–142. https://doi.org/10.1016/j.snb.2014.06.105.

(25) Muhammad Hafiz, S.; Ritikos, R.; Whitcher, T. J.; Md. Razib, N.; Bien, D. C. S.; Chanlek, N.; Nakajima, H.; Saisopa, T.; Songsiriritthigul, P.; Huang, N. M.; et al. A Practical Carbon Dioxide Gas Sensor Using Room-Temperature Hydrogen Plasma Reduced Graphene Oxide. *Sens. Actuators B Chem.* **2014**, *193*, 692–700. https://doi.org/10.1016/j.snb.2013.12.017.

(26) Zhou, Y.; Jiang, Y.; Xie, G.; Wu, M.; Tai, H. Gas Sensors for CO2 Detection Based on RGO–PEI Films at Room Temperature. *Chin. Sci. Bull.* **2014**, *59* (17), 1999–2005. https://doi.org/10.1007/s11434-014-0253-2.

(27) Smith, A. D.; Elgammal, K.; Fan, X.; Lemme, M. C.; Delin, A.; Råsander, M.; Bergqvist, L.; Schröder, S.; Fischer, A. C.; Niklaus, F.; et al. Graphene-Based CO2 Sensing and Its Cross-Sensitivity with Humidity. *RSC Adv.* **2017**, *7* (36), 22329–22339. https://doi.org/10.1039/C7RA02821K.

(28) Andò, B.; Baglio, S.; Di Pasquale, G.; Pollicino, A.; D'Agata, S.; Gugliuzzo, C.; C. Lombardo; Re, G. An Inkjet Printed CO2 Gas Sensor. *Procedia Eng.* **2015**, *120*, 628–631. https://doi.org/10.1016/j.proeng.2015.08.755.

(29) Willa, C.; Yuan, J.; Niederberger, M.; Koziej, D. When Nanoparticles Meet Poly(Ionic Liquid)s: Chemoresistive CO_2 Sensing at Room Temperature. *Adv. Funct. Mater.* **2015**, *25* (17), 2537–2542. https://doi.org/10.1002/adfm.201500314.

(30) Willa, C.; Schmid, A.; Briand, D.; Yuan, J.; Koziej, D. Lightweight, Room-Temperature CO_2 Gas Sensor Based on Rare-Earth Metal-Free Composites—An Impedance Study. *ACS Appl. Mater. Interfaces* **2017**, *9* (30), 25553–25558. https://doi.org/10.1021/acsami.7b07379.